AIChE Journal
DOI 10.1002/aic.15812

Sonochemical Effect Induced by Hydrodynamic Cavitation: Comparison of Venturi / Orifice Flow Geometries

Sandip K. Pawar,[1] Amit V. Mahulkar,[1] Kuldeep Roy,[2] Vijananand S. Moholkar,[2] Aniruddha B. Pandit[1]

[1] Dept. of Chemical Engineering, Institute of Chemical Technology (ICT), Matunga, Mumbai- 400 019, Maharashtra, India

[2] Dept.of Chemical Engineering, Indian Institute of Technology Guwahati, Guwahati – 781 039, Assam, India

* Corresponding author. Email: ab.pandit@ictmumbai.edu.in.

Abstract

This study presents comparative assessment of four cavitation devices (3 venturis and an orifice) in terms of cavitational yield. A 4-fold approach was adopted for assessment, viz. CFD simulations of cavitating flow, simulations of individual cavitation bubble dynamics, high speed photographs of cavitating flow and model reaction of potassium iodide oxidation. Influence of design parameters of cavitation devices on nature of cavitation produced in the flow was studied. Number density of cavitation bubbles in the flow and interactions among bubbles had critical influence on cavitation yield. Orifice gave the highest cavitational yield per unit energy dissipation in flow (despite lower working inlet pressure) due to low density of cavitation bubbles in flow. On contrary, occurrence of large cavitation bubble clouds in venturi flow had adverse effect on cavitational yield due to high interactions among cavitation bubbles resulting in inter-bubble coalescence and recombination of oxidizing radicals generated from cavitation bubbles.

Keywords: hydrodynamic cavitation, Weissler reaction, venturi, orifice, bubble dynamics

Received: Jan 31, 2017; Revised: Apr 15, 2017; Accepted: May 08, 2017

Introduction

Use of cavitation as a source of concentrated energy delivery for the chemical / physical and biological transformations is increasingly being studied owing to its ability to generate intense energy concentration (local high temperatures of ~ 10000 - 14000 K and pressures up to 100 - 400 MPa) at nearly ambient bulk processing conditions.[1] Transient cavitation makes energy available at extremely small temporal and spatial scales which is not available from any other source.[2] Thus, it is a highly efficient method for introducing energy in a system and also for intensification of diverse physical, chemical and biological processes.[3]

Hydrodynamic cavitation is generated by the passage of the liquid through a physical constriction such as an orifice plate[4] or a venturi[5] or a partially closed valve.[6] When the pressure at the constriction falls below the vapor pressure of the liquid, the liquid flashes thereby generating a number of cavities which subsequently collapse when pressure recovers downstream of the constriction. This phenomenon has been extensively studied, both experimentally and numerically.[7-11] Hydrodynamic cavitation has been used for several chemical engineering applications (involving physical / chemical processing) like waste water treatment,[12-14] water disinfection,[15] oxidation of alkylarenes[16] and emulsification and homogenization.[17] Recently, Ciriminna[18] has published a comprehensive review of hydrodynamic cavitation based technologies developed and commercialized by various companies for numerous applications. Moholkar[19] has recently published a review on mathematical models for chemical induced by hydrodynamic cavitation. Despite significant R&D efforts, the present methodologies for the design of hydrodynamic cavitation reactors have black box (trial and error) approach. A major limitation in modeling and optimization of hydrodynamic cavitation reactors is that most of the models for cavitation bubble dynamics have been developed for radial motion a single bubble, while actual cavitation phenomena occurring in the reactor essentially involves multi bubble fields with millions of strongly

interacting cavitation bubbles. The actual energy intensity and cavitation effect produced by multi-bubble fields could be significantly different than the cavitation intensity predicted by single bubble models. Interactions among the cavitation bubbles may also lead to asymmetric oscillations and collapse of the cavitation bubbles, in which the spherical geometry of the bubble is lost. Literature on cavitation bubble dynamics models that accounts for bubble/bubble and bubble/flow interactions in cavitating flows is rather limited. Moholkar and Pandit[20] have reported simulations of bubble dynamics in hydrodynamic cavitation reactors using continuum mixture model which essentially couples Rayleigh-Plesset equation for cavitation bubble dynamics to Navier-Stokes equations. In another paper, Kumar et al.[21] have reported flow regime maps for hydrodynamic cavitation reactors using modified continuum mixture model, in which Navier-Stokes equations were coupled with diffusion limited model of cavitation bubble dynamics (Toegel et al.[22]). The results of these studies clearly demonstrated the difference in the dynamics of a single cavitation bubble and a bubble cloud. The net cavitation intensity (quantified in terms of the peak temperature and pressure reached during cavitation bubble oscillations) produced by a cavitation bubble cloud was significantly smaller than an individual bubble. Capocelli et al.[23,24] have used the model of Kumar et al.[21] for theoretical estimation of chemical effects of hydrodynamic cavitation in the context of degradation of recalcitrant organic pollutants. In a recent study, Sarc et al.[25] have reported photographic study of cavitating flow (6000 frames per second at resolution of 946 × 248 pixels) in a cavitation test rig comprising four venturi type test sections. This study clearly revealed formation of cavitation clouds in the downstream region of venturi. The length and shedding frequencies of these cavitation clouds were a strong function of cavitation number. Sarc et al.[25] have used the experimentally measured pressure oscillations to quantify the cavitation intensity produced by the cavitation bubble clouds. The size (or length) of the cavitation cloud had significant effect on both magnitude and frequency of the

pressure oscillations. This result is an experimental confirmation of the adverse influence of inter-bubble interactions on net cavitation intensity produced in cavitation reactor.

In this work, we have compared the cavitation intensity or the sonochemical effect produced in hydrodynamic cavitation reactors employing different devices or flow geometries such as venturi and orifice. The experimental part of this study has two components: photographic analysis of the flow through venturis and orifice (fabricated using transparent materials), and conduction of a model sonochemical reaction. Photographic records of flow through cavitation devices like venturis with varying dimensions and orifice essentially give information of inception and development of cavitation phenomena in the flow. The model sonochemical reaction helps in direct quantification of the sonochemical or cavitational effect produced by each cavitation device or flow configuration. The experimental work is supported by single phase CFD simulations and bubble dynamics simulations using single-bubble model. Single phase CFD simulations predict the low pressure zone where cavitation can occur. This has been matched with photographic evidence of the cavitation occurring in venturi and orifice. Bubble dynamics simulations have predicted the cavitation intensity produced by single bubble in various geometries and operating conditions. It has been revealed that net yield of the model sonochemical reaction in different flow geometries does not concur with the simulations of cavitation bubble dynamics. This discrepancy has been explained on the basis of the nature of macroscopic cavitation phenomena occurring in different flow geometries involving, i.e. sizes of cavitation clouds generated in the flow and inter-bubble interactions in these clouds, due to which the net cavitation intensity in the flow is significantly different from the cavitation intensity predicted by single-bubble simulations. Venturi and orifice flow geometries have been compared on the basis of net sonochemical yield per unit energy dissipated in the flow. As explained in subsequent sections, this analysis has given a mechanistic insight into disparities

between microscopic (or single-bubble) and macroscopic (multi-bubble) cavitation phenomena, and its tangible manifestation in terms of the yield of a sonochemical reaction.

Before proceeding to the numerical model of hydrodynamic cavitation, a widely used dimensionless term 'cavitation number' (C_v) is briefly described here. C_v characterizes the cavitation event in a flow system in terms of global operating conditions and relate it with the cavitational intensity as follows:

$$C_v = \frac{P_2 - P_v}{\rho_L u_{throat}^2 / 2} \quad (1)$$

where P_2 is the fully recovered downstream pressure, P_v is the vapour pressure of the liquid at the operating temperature, ρ_L is the bulk liquid density, and u_{throat} is the liquid velocity at the throat of cavitation device. Cavitation is not generally possible unless the cavitation number is less than 1.0 and it is expected to be become more intense as the value of the cavitation number decreases. This term would be extensively used while discussing the results.

Flow and bubble dynamics simulations

Single phase steady state CFD simulations were performed for various geometries to identify low pressure zone, where cavity generation would occur and possible nuclei trajectory through the geometry. These results will further be compared with photographic evidence of cavitation cloud. CFD simulations and photographic evidence will later lead to qualitative analysis about number density of cavities. Major focus of simulations is on bubble dynamics which predicts chemical reactions occurring in the cavities as function of operating conditions and geometrical parameters.

Single phase CFD simulations

Single phase steady state 2D-axisymmetric CFD simulations were performed (water only) using FLUENT 6.3.[26] A schematic and a computational mesh used for venturi-2 is shown in Figure 1a. Structured mesh (fine mesh near the throat and coarse mesh away from the throat) was created with about 36000 cells for venturi and 48000 cells for orifice geometries. Standard k-ε turbulent model (standard wall function) was used with second order upwind discretization scheme for momentum, k and ε. Velocity inlet, pressure outlet, wall and axis boundary conditions were used at appropriate boundaries. Convergence was decided once all the residual dropped below 10^{-5} and fraction of mass balance difference in inlet and outlet was less than 10^{-4}. Once the flow is converged probable paths taken by nuclei was obtained by Discrete Phase Model (DPM) available in FLUENT 6.3. Nuclei movements were simulated massless particle flowing with water. The nuclei movement is affected by turbulence dispersion (stochastic discrete particle approach). Each nuclei trajectory was average of 20 particle tracks.

Simulations of individual cavitation bubble dynamics in each flow configuration

The radial dynamics of individual cavitation bubbles in the flow have also been simulated, along with associated physical effects, i.e. temperature and pressure peaks reached in the bubble and extent of water vapor entrapment in the bubble at the moment of transient collapse for various geometries. The radical species produced during transient cavitation (through thermal dissociation of the water vapor inside the bubble) in different flow geometries can be determined from the results of bubble dynamics simulations, as explained further. For this purpose, we have used diffusion-limited model for radial bubble dynamics proposed by Toegel *et al.*[22] which uses boundary layer approximation. This essentially is the

Lagrangian approach of simulating a cavitating flow with identification of individual cavitation bubbles.[27-29]

This model is based on the landmark paper of Storey and Szeri[30] which demonstrated that solvent vapor transport across the bubble interface during radial motion is essentially a diffusion-limited process. During the expansion of the bubble, significant evaporation occurs at the bubble interface, and the solvent molecules diffuse towards the bubble core. In the ensuing compression phase, the vapor molecules diffuse back towards the bubble interface and condense at the interface. However, in the final moments of bubble collapse, the bubble wall velocity becomes extremely high. As the time scale for diffusion of vapor molecules is higher than the time scale of motion of bubble interface, not all of the vapor molecules that have evaporated into the bubble can diffuse towards the bubble interface and undergo phase change. Moreover, the entire vapor molecules that approach bubble interface cannot condense at the interface, as the accommodation coefficient of the interface reduces drastically due to high velocity motion. This results in non-equilibrium phase change at the interface. As a consequence of these phenomena, solvent vapor entrapment occurs inside the bubble. The bubble compression is almost adiabatic, and the temperature and the pressure conditions inside the bubble reach extreme at the point of minimum bubble radius or maximum compression. At these conditions, the vapor molecules present inside the bubble dissociate to form numerous chemical species, some of which are radical species like $^{\bullet}OH$, $^{\bullet}O$ and $HO_2^{\bullet}$. These species can diffuse out of the bubble during compression. The bubble may also undergo fragmentation at the point of maximum compression (or minimum radius), with release of the chemical species into the liquid medium. This is essentially the sonochemical effect. Radicals and other species released from cavitation bubble can initiate/accelerate chemical reactions in the medium.

The diffusion limited model for cavitation bubble dynamics used in this study comprises of four ordinary differential equations (as listed in Table 1): 1. Keller-Miksis equation for radial motion of cavitation bubble; 2. Equation of diffusive flux of solvent vapor; 3. Equation for heat conduction across bubble interface; 4. Overall energy balance for the cavitation bubble as an open system. The transport parameters in the equations for diffusive flux and heat conduction, viz. thermal conductivity and diffusion coefficient, are determined at the bulk temperature of the liquid medium using kinetic theory of gases, i.e. Chapman-Enskog theory using Lennard-Jones 12-6 potential.[31-33] The thermodynamic data for the diffusion-limited model (i.e. properties of different species in the cavitation bubble) is given in Table 2. The vapor pressure of the solvent has been calculated using Antoine type correlation. This model does not account for rectified diffusion of non-condensable dissolved gases in the medium, across bubble interface, as the time scale for the diffusion at gas is much higher than the time scale for radial motion of cavitation bubble.

The time profile of bulk pressure in cavitating flow has been determined using the algorithm discussed in our previous work.[7,20] For convenience of the reader this algorithm is briefly reproduced as follows:

The velocity of the cavitating flow emerging from the throat of the venturi or orifice comprises of two components, viz. the mean flow velocity (U) and the turbulent velocity fluctuation. We consider here the time averaged turbulent fluctuating velocity ($\overline{u}'$). The instantaneous velocity in the flow can be written as:

$$u_t = U + \overline{u}' \qquad (2)$$

The flow velocity at the throat and in the pipe can be calculated using the volumetric flow rate of liquid and the cross-sectional area of throat and pipe. Knowing throat velocity, pipe velocity and the length of pressure recovery zone, the time of pressure recovery (τ) can be determined using Newton's equation. The length of pressure recovery zone in case of

venturis is the length of divergent section. In case of orifice flow, the length of pressure recovery zone is taken as 10× orifice throat diameter, on the basis of photographs of the cavitating flow. For determination of instantaneous turbulent fluctuating velocity, we have used reduced algorithm based on Kolmogoroff's hypothesis that the rate at which large eddies supply energy to the smaller eddies is proportional to reciprocal of the time scale of large eddies. Secondly, in view of results of Morrison *et al.*[34] that axial velocity variance (or mean square of axial velocity fluctuation) in orifice flow was much higher than the radial and azimuthal variance, we have considered turbulent velocity fluctuations only in the axial direction of flow. The magnitude of specific kinetic energy (per unit mass) of turbulent velocity fluctuations is ~ $\overline{u}'^2$, and the rate of energy transfer can be written as ~ $\overline{u}'/l$, where l is the size of the largest eddy in the flow. At steady state, the rate of turbulent energy supply equals the rate of energy dissipation, which can be written as: $\overline{u}'^2 \times \overline{u}'/l = \overline{u}'^3/l$.

The actual rate of turbulent energy dissipation per unit mass in the zone of pressure recovery downstream of the venture or orifice throat is estimated by product of permanent pressure head loss in the flow and volumetric liquid flow rate. The length scale of eddy (l) is estimated using Prandtl eddy model, viz. l = 0.08 d, where d is the conduit diameter. For the venturi configuration, the conduit diameter is taken as mean of throat and pipe diameter. For the orifice configuration, the conduit diameter is taken as throat diameter, as the expansion of flow in the zone of pressure recovery is negligible, as seen in the photographs of the cavitation zone downstream of the throat. The steady state frequency of turbulent fluctuating velocity (f_T) is determined as $\overline{u}'/l$.

Time profile of pressure recovery: Yan *et al.*[35] have demonstrated that pressure recovery profile in the flow of downstream of orifice or venturi is predominantly of linear nature, with turbulent pressure fluctuation superimposed over it. In view of this result, the time profile of pressure recovery is determined using following four steps:

1. The instantaneous bulk pressure in cavitating flow (P_t) is determined assuming linear pressure recovery in the flow from pressure at the throat (P_{throat}) to fully recovered pressure (P_2) – usually atmospheric pressure – in the pipe. For cavitation number ≤ 1, the bulk liquid pressure at throat is equal to the vapor pressure of the liquid (i.e. $P_{throat} = P_v$). The time required for full pressure recovery from P_{throat} to P_2 is τ. Thus, profile for P_t is written as:

$$P_t = P_{throat} + \frac{(P_2 - P_{throat})t}{\tau} \tag{3}$$

2. The instantaneous mean velocity of flow (u_t) corresponding to bulk pressure P_t is calculated by application of Bernoulli equation between venturi/orifice throat and the point in pressure recovery zone corresponding to time t:

$$u_t = \left\{ \left(P_{throat} + \rho_L u_{throat}^2 / 2 - P_t \right) / \rho_L / 2 \right\}^{1/2} \tag{4}$$

3. Turbulent fluctuations in mean flow velocity, with magnitude $\overline{u'}$ and frequency f_T, are assumed to have sinusoidal nature. The turbulent fluctuations are superimposed over the mean flow velocity as:

$$u_t^{new} = u_t + \overline{u'} \sin(2\pi f_T t) \tag{5}$$

4- The instantaneous bulk pressure corresponding to u_t^{new} is recalculated using Bernoulli equation as:

$$P_t = \rho_L u_{throat}^2 / 2 + P_{throat} - \rho_L \left(u_t^{new} \right)^2 / 2 \tag{6}$$

The time profile of bulk pressure in the cavitating flow thus obtained is substituted in the bubble dynamic equation.

Numerical solution: The four simultaneous ODEs of the diffusion-limited bubble dynamics model have been solved using Runge-Kutta 4th order - 5th order method with adaptive step size control.[36] The initial conditions for the numerical solution of the ODEs were: $t = 0$, $R = R_o$, $dR/dt = 0$, $N_w = 0$ and $T = T_o$. For all simulations, we have assumed an air bubble with R_o

= 10 μm. Bulk temperature of liquid (T_o) is taken as 303 K. Other physical properties of water are: P_v = 4.2 kPa, ρ_L = 1000 kg/m^3, ν = 10^{-6} m^2/s, σ = 0.072 N/m. The parameters for bulk pressure recovery profiles downstream of the venturi/orifice throat have been calculated as per procedure described in preceding section. These parameters are listed in Table 3.

Estimation of sonochemical effect: The temperature and pressure inside the bubble reach extreme at transient collapse (> 5000 K, > 100 MPa). Moreover, the bubble also attains minimum radius with extremely small volume. Thus, the concentrations of species inside the bubble are very high. As a result of these two factors, the rates of different chemical reactions occurring among different species inside the bubble are extremely fast. Considering this, we have assumed prevalence of thermodynamic equilibrium in the cavitation bubble all through the radial motion.[27] The simulations of cavitation bubble dynamics yield the peak temperature and pressure attained in cavitation bubble at transient collapse, along with the number of gas (N_2/O_2) and water vapor molecules present in the bubble at transient collapse. The equilibrium composition of chemical species (including radical species) resulting from thermal dissociation of vapor molecules in the bubble at peak temperature and pressure attained at transient collapse has been calculated using software FACTSAGE (online trial version available at www.factsage.com).

Experimental

Hydrodynamic cavitation set up

Schematic of the experimental setup used for hydrodynamic cavitation is as shown in Fig. 1b. The set-up consists of a closed loop circuit including a holding tank of capacity 15 L, a monoblock centrifugal pump of power rating 370 W, a bypass line to control flow through the main line which had the cavitation device (venturi/ orifice). The suction side of the pump is connected to the bottom of the tank. The discharge from the pump branches into two lines;

mainline and the bypass line. The main line consists of a transparent venturi or orifice for visual observation, which acts as a cavitating device. The mainline as well as the bypass line discharges into holding tank with their ends dipped well into the liquid in the holding tank to avoid any entrainment of air into suction line of the pump.

In the holding tank some ice bags were kept to control the temperature of the circulating liquid. Venturis were fabricated from transparent acrylic tubing. Dimensional details of each venturi and orifice is given in Table 3 (schematic of venturi-2 is shown in Fig. 1a). Orifice was made from acrylic sheet of 4 mm thickness with a hole of 2 mm diameter at its center. Pressure gauges are mounted to measure the upstream and downstream pressure of the cavitational device (P_1 and P_2). The downstream pressure (P_2) in all the cases was equal to atmospheric pressure.

High speed photographs of the flow downstream of the throat in all cavitation devices can provide direct information regarding nature and characteristics of the cavitation phenomena occurring in the flow. Cavitation phenomena occurring in the pressure recovery zone downstream of the throat in venturi and orifice was photographed at the shutter speed of 1/1250 s (or 0.8 milliseconds) using a digital camera (Canon Powershot S31S). For the three venturis, the divergent section downstream of throat was illuminated using bright field illumination technique. In case of orifice dark field illumination technique was used for obtaining photographs of region (approx. 2 in. length) downstream of throat. Illumination was provided using 100 W tungsten incandescent lamp with appropriate diffuser to avoid intense reflection from outer surface of venturi/orifice. Photographs were obtained in macro-mode to shoot close object (< 10 cm) without any magnification.

Assessment of cavitation intensity using model reaction

Transient collapse of cavitation bubbles generates radical species such as $H^{\bullet}$, $O^{\bullet}$, $^{\bullet}OH$ and $HO_2^{\bullet}$. These radicals can initiate/accelerate chemical reactions in the bulk liquid medium. This is essentially the sonochemical effect, which is a function of cavitation intensity produced in the system. Relative cavitation intensity produced by each of the cavitation device was assessed using a model reaction viz. oxidation of potassium iodide (KI) to liberate iodine (I_2). This reaction, also known as Weissler reaction,[37] is a standard dosimeter for evaluation of the cavitational yield.

The overall cavitational yield of the hydrodynamic cavitation reactor depends on several factors such as number of cavitation bubbles generated in the flow, intensity of transient collapse of individual cavitation bubbles and radical production from them, the interaction among the cavitation bubbles and net utilization of the radicals towards the model reaction. The cavitation bubbles can grow out of nuclei already present in the liquid. These nuclei could be gas pockets trapped in the crevices of the solid boundaries in the cavitation reactor or free floating tiny bubbles. Moreover, the dissolved gas in the liquid can also get released with fall in bulk pressure generating cavitation bubbles in the flow. Thus, initial dissolved gas in the liquid is a major source of cavitation bubbles.

Similar to acoustic cavitation, degassing also takes place in hydrodynamic cavitation. The gas bubbles released from the liquid are seen at the exit of main line housing the cavitation element (venturi/orifice). The net degassing ceases after some time (~ 3-4 min) when the amount of dissolved gases in liquid is reduced to an extent that a dynamic equilibrium is reached between the net rate of degassing due to cavitation and re-dissolution of gases in the holding tank open to atmosphere. Since the amount of dissolved gases greatly determines the number of cavities formed and also the overall cavitational yield, it is essential to maintain similar dissolved gas concentration for all the experimental runs. For this, initially 6 L of

distilled water was circulated through the cavitational device for about 5 min and when bubbles were not seen in the discharge line, 120 g of pre-dissolved KI was added to make 2% KI solution (wt% basis). This was considered as the time $t = 0$. In a cavitation reactor, the extent of chemical transformation is a function of probability of interaction between the reactant molecules and the radicals generated from the transient cavitation bubbles.[38] Cavitation phenomenon itself being a sporadic event in both time and space domain, the probability of interaction between reactants and radicals is a function of concentration of the reactant (in the present context KI molecules).[39] This essentially implies that the initial concentration of KI should be sufficiently in excess such that it remains practically constant during experiment and the I_2 liberation through KI oxidation is essentially a function of rate and quantity of radical generation by transient cavitation bubbles in each flow geometry.

The temperature of the circulating liquid was maintained in the range of 30^{o}C to 35^{o}C. Samples for Iodine analysis were collected at 3, 6, 9, 12, 15 & 20 min of operation. Samples were analyzed for their absorbance with UV spectrophotometer at 354 nm wavelength for the estimation of liberated free iodine concentration. Experiments with venturi-2 and Orifice were conducted in trpilicate, while for Venturi-1 and Venturi-3 were conducted in duplicate. The same experimental procedure was repeated for venturi and orifice as well to compare the cavitational yield in each of the configuration. Experimental conditions are summarized in Table 4.

The maximum upstream pressure (P_1) that could be obtained in the current setup was 320 kPa gauge (completely closed bypass valve position). However, depending on the flow geometries of different cavitation devices, the liquid flow rate with actual or working inlet pressure obtained for each device was different. The liquid flow rates and working inlet pressures for the four cavitation devices are listed in Table 3. The throat diameter for venturi 3 is large (8 mm) with a very small convergent angle (2^o) in the upstream region. As a result,

the liquid flow rate through venturi 3 was significantly higher than other flow geometries with concurrent reduction in actual or working inlet pressure of the flow. On the other hand, the liquid flow encountered sudden and sharp contraction in the upstream region of orifice. This resulted in large pressure head loss in the upstream region with reduction in the working inlet pressure. As the orifice to pipe diameter ratio was very small (0.08), the head loss coefficient was ~ 0.45, and the working inlet pressure was reduced to 233 kPa. The flow rate corresponding to this working pressure was also the smallest among all flow geometries, i.e. 67 mL/s.

Results and Discussions

Photographic study of cavity inception and cloud formation

Figures 2a-2c and 2d-2f show photographs of flow in the immediate downstream region of venturi and orifice throat respectively, with increasing upstream pressure. This region is essentially the zone for occurrence of cavitation phenomena. Photographs in the first row (Figure 2a and 2d) show cavitation inception in both venturi and orifice. Cavity inception was observed for upstream pressure (or pump discharge pressure) of 180 kPa (throat velocity = 16.0 m/s, C_v = 0.76) in venturi and upstream pressure of 240 kPa (throat velocity = 13.9 m/s, C_v = 1.01) in case of orifice. At these operating conditions the cavities were seen to form only intermittently. Continuous formation of cavities occurred when the upstream pressure is increased to 200 kPa (throat velocity = 20.7 m/s, C_v = 0.45) in venturi and to 280 kPa for orifice (throat velocity = 15.4 m/s, C_v = 0.83) as shown in Figure 2b and 2e. In the case of venturi, the cross sectional flow area converges smoothly due to which laminarization of flow takes place. This results in the lowering of the turbulence intensity at the throat. In orifice, due to sudden change in liquid velocity, owing to sudden contraction and expansion of flow, higher liquid phase turbulence is generated. Thus, in venturi the continuous cavity formation

occurs at relatively lower cavitation number of 0.45 (i.e. higher pressure and velocity) as compared to that in orifice (cavitation number of 0.83). The difference in nature of cavitation phenomena occurring in venturi and orifice for similar cavitation number, as seen from Figure 2, clearly demonstrates that cavitation number by itself cannot be a yardstick for performance of the cavitation device. Several other factors also have critical influence on the cavitation intensity produced by the cavitation device. In the present context, the turbulence generated in the flow due to pressure head loss in both upstream and downstream region of the throat influences the nature of cavitation phenomena in venturi and orifice. Similar observations have also been made by Sarc et al.[25] about cavitation number being insufficient measure for quantification of cavitation intensity. Sarc et al.[25] have pointed out several other factors, viz. system geometry, temperature, dissolved gas in liquid medium and ease of cavitation nucleation, that affect the macroscopic cavitation intensity produced in the system.

For maximum upstream pressure of 420 kPa, fully developed cavitating flow with permanent cavitation clouds were observed for throat velocity of 28.9 m/s and C_v = 0.23 for the venturi (Figure 2c). For the orifice flow as well, fully developed cavitation clouds are observed for maximum upstream pressure of 320 kPa (throat velocity = 21.4 m/s and C_v = 0.42). However, the size of these cavitation bubble clouds, as observed in Figure 2f, is far smaller than the cavitation clouds in venturi. This essentially points towards significantly smaller number density of cavitation bubbles in the orifice flow. This effect is consequence of large pressure head loss of the flow in the upstream region of orifice plate due to sudden contraction of the flow. This pressure head loss is manifested in terms of generation of significant turbulence in the flow. The liquid velocity generated at the throat is relatively much smaller as compared to venturi. These factors are essentially reflected in higher cavitation number corresponding to the cavitation inception, as compared to venturi flow. Nonetheless, this attribute of the cavitating flow through orifice has worked towards

enhancement of the net sonochemical effect produced in the reactor, as explained in greater detail subsequently.

CFD Simulation results

Figure 3 shows the paths taken by the cavitation nuclei as they flow through the cavitational zone overlapped over the pressure contours in venturi and orifice as obtained from CFD simulations. The scale of pressure contours shown in Figure 3 was clipped, such that it shows region with absolute pressure < 50 kPa, i.e. region of probable cavitation (the maximum value of absolute pressure is 50 kPa to minimum value of 4 kPa i.e. vapor pressure of water). For venturi, the results show that the entire cross sectional area in the throat and part of divergent section is covered with this low pressure region. The value of 50 kPa was chosen for the above analysis because as shown in Figure 3, the vapor cloud (in Figure 2) is seen to exist till the zone where the pressure is approximately 50 kPa. It is seen that, in the case of venturi the low pressure zone covers the entire volume of throat and it also extends into the diverging section up to ~15 mm. In case of orifice the low pressure region is limited only to the leading edge of the orifice hole. Thus, in venturi all nuclei pass through the low pressure region while for orifice very few nuclei flow through the low pressure region (probable cavitation region). As a result, in venturi very large numbers of cavities are created and the entire cross sectional area of the throat is occupied by the cavities. For orifice, very few cavities are created near the perimeter of holes. The photographs of cavitating flow depicted in Figure 2c also show very dense (darker) cloud of cavities in venturi over the entire cross sectional flow area, whereas for orifice (Figure 2f) very faint (brighter) cloud of cavities originating from the periphery of the hole is observed. In the case of the venturi, the cavity cloud is very clearly visible in Figure 2c as the number density of cavities is very high compared to that in orifice.

In the case of orifice, since the cavities are formed only along the periphery of the hole, the increase in the perimeter to area ratio is expected to improve the sonochemical effect produced by cavitating flow, which is manifested in terms of enhancement in yield of the model reaction, i.e. iodine liberation from KI oxidation. Moholkar *et al.*[40] reported that maximum KI oxidation was obtained when the perimeter to open area ratio was highest for various configurations of orifice with multiple holes employed in their study. The behavior of cavities generated from the leading edge of orifice, where low pressure region is created, was also observed by Sato and Saito.[41] This observations goes against the general expectation that low pressure region in orifice is formed at vena contracta (which lies downstream of the orifice plate). As mentioned earlier, in venturi the cavity cloud extend to ~15 mm after the throat. But the vapor formed in orifice is very much under predicted by CFD. The CFD results show all the cavities are collapsing within the thickness of the orifice plate (span of 4 mm only). However, the photographs of cavitating flow downstream of orifice throat (Figure 2e) show cavitation bubble clouds to extend much beyond the orifice plate. The essential difference between the cavitation in the two devices is in the number density of cavities, i.e. vapor volume fraction, as discussed earlier. When the number density of cavities is low, the cavity-cavity interactions are limited but for the higher number density of cavities, the cavity-cavity interaction is very dominant and the cavities form a cluster or a cloud. It may also be noted that large number density of cavitation bubbles in the flow can lead to strong interaction and coalescence among bubbles. Thus, the cavitation bubbles may lose their sphericity, which results in marked reduction in the intensity of their transient collapse, i.e. the temperature and pressure peaks attained in the bubble at transient collapse, and the extent of generation of radicals through thermal dissociation of vapor entrapped in cavitation bubbles. This has adverse effect on the sonochemical effect produced by the cavitating flow as explained further.

Simulations of individual cavitation bubble dynamics

Representative results of simulations of radial motion of 10 μm air bubble in the cavitating flow through venturi-1 and orifice are shown in Figures 4 and 5, respectively. Summary of the simulations results for the four cavitation devices considered in this study are presented in Table 5. Results presented in Table 5 include the peak temperature and pressure reached in the cavitation bubble at transient collapse, the number of water vapor molecules entrapped in the bubble at transient collapse, and the mole fractions of N_2, O_2 and water vapor molecules in the bubble at transient collapse. As noted earlier, the equilibrium mole fraction of different species resulting from thermal dissociation of gas and vapor molecules inside the bubble has been calculated using Gibbs free energy minimization. These results have also been presented in Table 5. The similarities and differences in the radial motion of cavitation bubble in venturi and orifice are evident from Figures 4 and 5. The cavitation bubble undergoes expansion to more than 15× its original size in both flow geometries. This is accompanied by large evaporation of water vapor in the bubble. At the final moments of transient compression, not all vapor can escape the bubble resulting in entrapment of some fraction of water vapor in the bubble. In fact as revealed from mole fractions of gas and vapor molecules in the bubble at transient collapse, the bubble becomes supersaturated with water vapor at transient collapse. Thermal dissociation of nitrogen, oxygen and water molecules generates large number of chemical species, the dominant among which are radical species, viz. $^{\bullet}OH$, $H^{\bullet}$, $O^{\bullet}$ and $HO_2^{\bullet}$. Several nitrogen containing species also form; however, the mole fraction of these species is relatively far smaller.

Due to smaller working inlet pressure, the temperature peak attained at transient collapse of cavitation bubble in orifice flow is relatively smaller than venturi flow. Moreover, as seen from Table 5, the magnitude as well as frequency of the turbulent pressure fluctuations in the

venturi flow is much higher than orifice flow. As a result, the cavitation bubble in venturi flow is seen to undergo several large amplitude oscillations, which last for more than 60% of the total time for pressure recovery. This essentially indicates that the active cavitation zone in venturi flow occupies significant fraction of the divergent section downstream of the throat. On the other hand, the cavitation bubble undergoes a single large growth and transient collapse, followed by few small amplitude after bounces, in orifice flow. These oscillations of cavitation bubble last for ~20% of the total time for pressure recovery. Thus, the active cavitation zone for orifice flow extends to relatively much shorter distance downstream of orifice throat. Due to relatively smaller temperature peak attained at transient collapse, the equilibrium mole fraction of the radicals generated from transient collapse of cavitation bubbles in orifice flow is smaller than venturi 1 and 2. The least temperature peak is obtained for venturi 3, which has least working inlet pressure due to large volumetric flow rate as noted earlier. Remarkably, the cavitation bubble is seen to undergo transient motion and collapse in all four flow geometries giving rise to the sonochemical effect of radical formation.

Experimental results

The extent of iodine liberation in cavitating flow represents the cavitational (or sonochemical) yield. We have compared the iodine liberation in four cavitation devices for same operation period of 20 min and energy consumed by the system for operation. Figure 6a shows iodine liberated as function of energy consumed by the cavitation device. For 20 min of operation, the final iodine concentrations attained in hold tank of hydrodynamic cavitation reactor for four cavitation devices were as follows: Venturi 1: 0.82 mg/L, venturi 2: 0.79 mg/L, venturi 3: 0.49 mg/L, orifice: 0.65 mg/L. For 6 L working volume of KI solution, the

above concentrations correspond to net I_2 yield of 4.94, 4.77, 2.91 and 3.90 mg, respectively, for the four cavitation devices stated above.

In order to compare the efficiencies of four cavitation devices, we have extended the analysis in terms of iodine yield per unit energy input. The pump used in the present study had low power rating (0.37 kW) and low electrical to hydraulic energy conversion efficiency (~ 10%). Considering this, we have based calculation of cavitational or sonochemical yield on actual energy dissipated in flow downstream of the throat of cavitation device. The energy dissipation in cavitating flow has been determined by product of net pressure drop in the downstream region, the volumetric flow generated by the device and the time of operation. A representative calculation of the cavitation yield is presented in Appendix A. The cavitational yield for the four cavitation devices were determined as follows: venturi 1: 0.12 mg I_2/kJ, venturi 2: 0.11 mg I_2/kJ, venturi 3: 0.039 mg I_2/kJ and orifice: 0.17 mg I_2/kJ. These trends are depicted in Figure 6b.

Comparative evaluation of geometrical features, cavitation yield and nature of cavitation phenomena in venturi-1 and venturi-2 (as demonstrated in photographs in Figure 7) reveal an interesting feature of the macroscopic (or multibubble) cavitation occurring in these devices. The throat diameter and cavitation number for venturi-1 and venturi-2 were same. The divergence angle for venturi-1 (12^o) is twice that of venturi-1 (6^o). The photographs of the cavitation zone downstream of the throat in venturi-1 and venturi-2, shown in Figure 7, reveal significantly larger cavitation cloud for venturi-2. However, the cavitation (or sonochemical) yield in these devices is practically same. This clearly indicates that cavitation intensity produced in the device does not vary proportionately with the size of cavitation cloud. This discrepancy is attributed to strong interbubble interactions in large cavitation clouds that adversely affect the net cavitation intensity. Similar observation is also made by Sarc et al.[25] and Petkovsek et al.[42] where pressure fluctuations resulting from

oscillation/collapse of cavitation clouds were significantly affected by variation in divergence angles of the venturi sections.

Concurrent analysis of experimental and simulations results

Analysis presented in preceding section has revealed orifice to be the most efficient cavitation device in terms of iodine liberation per unit energy dissipation in the flow. This result is an anomaly since the intensity of transient cavitation was higher for both venturi-1 and venturi-2, as per the simulations of cavitation bubble dynamics presented in Table 5. The CFD simulations of cavitating flow also indicated much higher number density of cavitation bubbles for venturi flow, which essentially pointed at higher cavitation intensity. On the other hand, in orifice flow large pressure head loss occurred in the upstream region itself, as a result of which the net energy dissipation in cavitating flow reduced sharply. CFD simulations also predicted much smaller number density of cavitation bubbles for orifice flow. Despite lesser number density of cavitation bubbles and smaller energy dissipation in cavitating flow, the cavitational yield in the orifice is marked larger than all venturi configurations. A plausible explanation for this observation can be given as follows: the photographs of cavitating flow in venturi and orifice presented in Figure 2 show far larger cavitation bubble clouds in the divergent section of venturi as compared to orifice. These bubble clouds are seen to occupy large fraction of the volume of divergent section of venturi and nearly entire cross-sectional area of the flow. High number density of cavitation bubbles in the divergent section of venturi results in strong bubble/bubble interactions. Coalescence among cavitation bubbles in close vicinity is also likely to occur, which gives rise to larger cavitation bubbles that collapse with lesser intensity. Close vicinity of cavitation bubbles can also trigger recombination of the radicals produced during transient collapse of these bubbles, which essentially is a loss of possible sonochemical effect. These features essentially result in marked reduction in cavitational yield. The photographs of cavitating flow in orifice show far

smaller cloud of cavitation bubbles. Due to smaller number density of cavitation bubbles, inter-bubble interaction is far less, which results in lesser coalescence among cavitation bubbles and prevalence of individual cavitation bubble dynamics. This obviously augments intensity of transient collapse of individual bubbles owing to symetric collapse of cavity. Recombination of radicals due to close neighborhood of cavitation bubbles is also expected to reduce, which results in their higher and effective utilization for KI oxidation. The net manifestation of these facets of cavitating flow through orifice is higher iodine liberation and greater cavitational yield per unit energy input.

Comparison of cavitation yield among three venturis vis-à-vis photographic analysis of flow and simulations of cavitation bubble dynamics also asserts the adverse effect of interactions among cavitation bubbles on lowering of the cavitation yield. Although the working inlet pressure for venturi 1 and 2 is almost similar, the rate of pressure recovery in venturi 1 is much faster due to larger divergence angle (12^o) of the downstream region than venturi 2 (divergence angle of 6^o). Thus, the intensity of transient cavitation, as predicted by simulations of individual cavitation bubble dynamics, is higher for venturi 1. This essentially points to larger cavitation yield in venturi 1. But contrary to this expectation, the cavitation yield in venturi 1 is only marginally (~ 10%) higher than venturi 2. An explanation for this discrepancy can also be given along similar lines of inter-cavitation bubble interactions. Due to larger divergence angle and shorter length of divergent section, the volume of the pressure recovery zone in venturi 1 is significantly smaller than venturi 2. This results in larger number density of bubbles in pressure recovery zone (or active cavitation zone) leading to higher interaction / coalescence among cavitation bubbles, recombination of oxidizing radicals produced by adjacent cavitation bubbles, and concurrent reduction in net cavitation intensity. The cavitational yield per unit energy input is adversely affected due to these facets.

In case of venturi 3, large throat dia. of 5 mm along with very small convergence angle of 2^o in the upstream region results in very large volumetric flow rate of 377 mL/s. The maximum inlet pressure obtained for these conditions is just 160 kPa. The energy dissipation in cavitating flow in the downstream region of venturi 3 is relatively much smaller as compared to other venturis. The number density of bubbles generated in the flow are also expected to be lower than venturi 1 and 2. Due to smaller energy dissipation in the flow, the intensity of transient collapse of these cavitation bubbles in venturi 3 is also the lowest among all 4 cavitation devices, as seen from the simulations results presented in Table 5. As a consequence of these factors, cavitating flow through venturi 3 gives least cavitational yield of 0.039 mg I_2/kJ.

Conclusion

The present study has attempted to make comparative assessment of sonochemical effect or cavitational yield of four cavitation devices with different flow geometries. A 4-fold approach was adopted for comparative assessment, viz. CFD simulations of cavitating flow using FLUENT 6.3, simulations of individual cavitation bubble dynamics using diffusion limited model, high speed photographs of cavitating flow in downstream region of cavitation devices and a model reaction of KI oxidation to liberate I_2. Effects of design parameters of cavitation device and operating conditions on the net cavitational yield was assessed iodine liberation through KI oxidation by radicals produced by transient cavitation bubbles. The efficiency of cavitation devices was adjudged on the basis of iodine liberated per unit energy dissipation in cavitating flow. Concurrent analysis of experimental results and simulations has brought forth important facets of cavitation phenomena produced by different flow geometries. The design parameters of the flow geometries (or cavitation devices) such as convergence/divergence angle in upstream/downstream section and relative diameters of

throat and inlet pipe have strong influence on nature and characteristics of resultant cavitation phenomena. Overall efficiency of cavitation devices in producing sonochemical effect is revealed to be a major function of interactions among cavitation bubbles, which in turn depend on number density of bubbles in the flow – and not on the intensity of collapse of individual cavitation bubbles. This is evident from the highest cavitational yield for orifice, despite smaller working inlet pressure (due to significant head loss in the upstream region of cavitation device) and low flow rate than venturi 1 and 2. On the other hand, excessively large cavitation clouds (with large cavitation bubble density) produced in both venturi 1 and 2 worked towards reduction in net sonochemical effect and cavitational yield due to strong destructive interactions among cavitation bubbles. High divergence angle in venturi 1 resulted in faster pressure recovery for almost same inlet pressure in cavitating flow than venturi 2. However, due to smaller volume of the pressure recovery zone (i.e. the divergent section of venturi), higher interactions among cavitation bubbles resulted in reduction of cavitational yield. Large throat diameter in venturi 3 resulted in the highest cavitating flow rate but with far reduced inlet pressure that resulted in marked reduction in cavitation intensity.

In summary, the results of this study have vividly demonstrated links between design and operational parameters of flow geometries or cavitation devices on nature and characteristics of the cavitation phenomena produced in the hydrodynamic cavitation reactor and its manifestation on sonochemical effect or cavitational yield from the reactor. We believe that results of this study would provide crucial inputs for effective design and optimization of the cavitation devices in hydrodynamic cavitation reactor so as to boost the net efficiency of these reactors.

Notation

θ = characteristic vibrational temperature(s) of the species, K

ν = kinematic viscosity of liquid, m^2/s

σ = surface tension of liquid, N/m; Lennard Jones force constant (molecular diameter), m

λ = thermal conductivity of bubble contents, W/m K

κ = thermal diffusivity of bubble contents, m^2/s

θ = vibrational temperature, K

τ = time for full pressure recovery, s

ε/k = Lennard-Jones force constant (reduced temperature), K

ρ_L = density of the liquid, kg/m^3

$\overline{u'}$ = turbulent fluctuating velocity, m/s

c = velocity of sound in bulk liquid medium, m/s

$C_{V,i}$ = heat capacity at constant volume for species I, J/mol K

C_W = concentration of water vapor molecules in the bubble, mol/m^3

$C_{W,R}$ = concentration of water vapor molecules at the bubble wall or gas–liquid interface, mol/m^3

dR/dt = bubble wall velocity, m/s

D_W = diffusion coefficient of water vapor, m^2/s

f_i = translational and rotational degrees of freedom, (-)

f_T = instantaneous frequency of the turbulent fluctuating velocity, m/s

h = van der Waal's hard core radius, m

h_W = molecular enthalpy of water vapor, J/mol

k = Boltzmann constant, J/mol K

N_{tot} = total number of molecules (gas + vapor) in the bubble, (-)

N_W = number of water vapor molecules in the bubble, (-)

P_2 = recovery pressure downstream of orifice/venture throat, Pa

P_{throat} = bulk liquid pressure at the throat of venturi/orifice, Pa

Q = heat conducted across bubble wall, W

R = radius of the bubble, m

T = temperature of the bubble contents, K

T = time, s

T_o = ambient (or bulk liquid medium) temperature, K

u_{pipe} = flow velocity of pipe, m/s

U_{throat} = flow velocity of throat, m/s

U_W = internal energy of water vapor molecules, J/mol

x_{N2} = mole fraction of nitrogen molecules in the bubble, (-)

x_{O2} = mole fraction of oxygen molecules in the bubble, (-)

x_W = mole fraction of water vapor molecules in the bubble, (-)

Literature Cited

1. Hilgenfeldt, S., Brenner M., Grossmann S., Lohse, D. Analysis of Rayleigh-Plesset dynamics for sonoluminescing bubbles. *J Fluid Mech.* 1998;365:171-204.
2. Moholkar VS, Warmoeskerken MMCG. Integrated approach to optimization of an ultrasonic processor. *AIChE J*. 2003; 49(11): 2918–2932.
3. Choudhury HA, Goswami PP, Malani RS, Moholkar VS. Ultrasonic biodiesel synthesis from crude *Jatropha curcas* oil with heterogeneous base catalyst: Mechanistic insight and statistical optimization. *Ultrason. Sonochem.* 2014;21:1050–1064.
4. Yan Y, Thorpe RB. Flow regime transitions due to cavitation in the flow through an orifice. *Int J Multiphase Flow*. 1990;16:1023-1045.
5. Weninger KR, Camara CG, Putterman SJ. Energy focusing in a converging fluid flow: Implications for sonoluminescence. *Phys Rev Lett*. 1999;83:2081-2084.
6. Pandit AB, Joshi JB. Hydrolysis of fatty oils: effect of cavitation. *Chem Eng Sci*. 1993;48:3440-3442.
7. Moholkar VS, Pandit AB. Bubble behavior in hydrodynamic cavitation: effect of turbulence. *AlChE J*. 1997;43:1641-1648.
8. Patil MN, Pandit AB. Cavitation – a novel technique for making stable nano-suspensions. *Ultrason Sonochem.* 2007;14(5):519-530.
9. Gogate PR, Pandit AB. A review and assessment of hydrodynamic cavitation as a technology for the future. *Ultrason Sonochem*. 2005;12:21-27.
10. Moholkar VS, Pandit AB. Numerical investigations in the behaviour of one-dimensional bubbly flow in hydrodynamic cavitation. *Chem Eng Sci*. 2001;56(4):1411-1418.

11. Kumar PS, Kumar MS, Pandit AB. Experimental quantification of chemical effects of hydrodynamic cavitation. *Chem Eng Sci.* 2000;55(9):1633-1639.

12. Dular M, Griessler-Bulc T, Gutierrez-Aguirre I, Heath E, Kosjek T et al. Use of hydrodynamic cavitation in (waste)water treatment. *Ultrason. Sonochem.* 2016;29:577-588.

13. Bagal MV, Gogate PR. Degradation of diclofenac sodium using combined processes based on hydrodynamic cavitation and heterogeneous photocatalysis. *Ultrason Sonochem.* 2014;21:1035-1043.

14. Sivakumar M, Pandit AB. Wastewater treatment: a novel energy efficient hydrodynamic cavitational technique. *Ultrason Sonochem.* 2002;9:123-131.

15. Jyoti KK, Pandit AB. Water disinfection by acoustic and hydrodynamic cavitation. *Biochem Eng J.* 2001;7(3):201-212.

16. Ambulgekar GV, Samant SD, Pandit AB. Oxidation of alkylarenes to the corresponding acids using aqueous potassium permanganate by hydrodynamic cavitation. *Ultrason Sonochem*. 2004;11:191-196.

17. Freudig B, Tesch S, Schubert H. Production of Emulsions in High-Pressure Homogenizers – Part II: Influence of Cavitation on Droplet Breakup. *Eng Life Sci.* 2003;3:266-270.

18. Ciriminna R, Albanese L, Meneguzzo F, Pagliaro M. Wastewater remediation via controlled hydrocavitation. *Environ Rev.* (2016) doi: 10.1139/er-2016-0064.

19. Moholkar VS. Mathematical models for sonochemical effects induced by hydrodynamic cavitation. In: M. Ashokkumar. Handbook of Ultrasonics and Sonochemistry. Singapore:Springer Science + Business Media, 2015:1-48.

20. Moholkar VS, Pandit AB. Modeling of hydrodynamic cavitation reactors: a unified approach. *Chem Eng Sci.* 2001;56:6295–6302.

21. Kumar P, Khanna S, Moholkar VS. Flow regime maps and optimization thereby of hydrodynamic cavitation reactors. *AIChE J.* 2012;58:3858–3866.

22. Toegel R, Gompf B, Pecha R, Lohse D. Does water vapor prevent upscaling sonoluminescence? *Phys Rev Lett.* 2000;85:3165-3168.

23. Capocelli M, Prisciandaro M, Lancia A, Musmarra D. Modeling of cavitation as an advanced wastewater treatment. *Desalin Water Treat.* 2013;51:1609-1614.

24. Capocelli M, Musmarra D, Prisciandaro M, Lancia A. Chemical effect of hydrodynamic cavitation: simulation and experimental comparison. *AIChE J.* 2014;60:2566-2572.

25. Sarc A, Stepisnik-Perdih T, Petkovsek M, Dular M. The issue of cavitation number value in studies of water treatment by hydrodynamic cavitation. *Ultrason Sonochem.* 2017;34:51-59.

26. *ANSYS I. ANSYS FLUENT Theory Guide 6.3*. Lebanon NH (USA):ANSYS Inc., 2006.

27. Krishnan JS, Dwivedi P, Moholkar VS. Numerical investigation into the chemistry induced by hydrodynamic cavitation. *Ind Eng Chem Res.* 2006;45:1493-1504.

28. Kumar KS, Moholkar VS. Conceptual design of a novel hydrodynamic cavitation reactor. *Chem Eng Sci.* 2007;62:2698-2711.

29. Kumar P, Moholkar VS. Numerical assessment of hydrodynamic cavitation reactors using organic solvents. *Ind Eng Chem Res.* 2011;50:4769-75.

30. Storey BD, Szeri AJ. Water vapour, sonoluminescence and sonochemistry. *Proc R Soc London: Ser A*. 2000;456:1685-1709.

31. Hirschfelder JO, Curtiss CF, Bird RB. *Molecular Theory of Gases and Liquids*. New York:Wiley, 1954.

32. Condon EU, Odishaw H. *Handbook of Physics*. New York:McGraw Hill, 1958.

33. Reid RC, Prausnitz JM, Poling BE. *Properties of Gases and Liquids*. New York:McGraw Hill, 1987.

34. Morrison GL, Deotte RE, Nail GH, Panak DL. Mean velocity and turbulence fields inside a β= 0.5 orifice flowmeter. *AIChE J.* 1993;39(5):745-756.

35. Yan Y, Thorpe RB, Pandit AB. Cavitation noise and its suppression by air in orifice flow. In *Symposium on Flow-Induced Noise*, Chicago, IL 1988;6: 25-39.

36. Press WH, Teukolsky SA, Flannery BP, Vetterling WT. *Numerical Recipes*, New York: Cambridge University Press, 1992.

37. Weissler A, Cooper HW, Snyder S. Chemical effect of ultrasonic waves: oxidation of potassium iodide solution by carbon tetrachloride. *J Am Chem Soc.* 1950;72:1769-1775.

38. Sivasankar T, Paunikar AW, Moholkar VS. Mechanistic approach to enhancement of the yield of a sonochemical reaction. *AIChE J.* 2007;53:1132–1143.

39. Zupanc M, Kosjek T, Petkovsek M, Dular M, Kompare B, Sirok B, Strazar M, Heath E. Shear induced hydrodynamic cavitation as a tool for pharmaceutical micropollutants removal from urban wastewater. *Ultrason Sonochem.* 2014;21:1213-1221.

40. Moholkar VS, Kumar PS, Pandit AB. Hydrodynamic cavitation for sonochemical effects. *Ultrason Sonochem.* 1999;6(1): 53-65.

41. Sato K, Saito Y. Unstable Cavitation behavior in a circular-cylindrical orifice flow. *JSME Int J Ser B Fluids Therm Eng.* 2002;45(3):638-645.

42. Petkovsek M, Zupanc M, Dular M, Kosjek T, Heath E, Kompare B, Sirok B. Rotation generator of hydrodynamic cavitation for water treatment. *Sep Purif Technol.* 2013;118:415-423.

List of Figure Captions

Figure 1: (a.1) Schematic diagram of the venturi 2. (a.2) Mesh used for CFD simulations and plane for nuclei injection. (b) Schematic diagram of the hydrodynamic cavitation closed loop set-up.

Figure 2: Photographs of cavitating flow downstream of venturi / orifice throat. Inception of cavitation phenomena is visible in Figs. (a) and (d) for venturi (for inlet pressure 180 kPa) and orifice (for working inlet pressure 240 kPa), respectively. Fully developed cavitation bubble clouds for the highest inlet pressure of 320 kPa for venturi and orifice are visible in Figs. (c) and (f).

Figure 3: Cavitation bubble paths or trajectories overlapped over the pressure contours in (a) venturi, and (b) orifice. The pressure contours are clipped so that maximum pressure is 50 kPa and minimum pressure is 4 kPa to indicate probable cavitation zone.

Figure 4: Results of simulations of radial dynamics of an air cavitation bubble (R_o = 10 μm) in cavitating flow downstream of throat in venturi - 1. Time history of: (A) normalized radius (R/R_o) of the bubble, (B) temperature inside the bubble, (C) water vapor molecules in the bubble, and (D) pressure inside the bubble.

Figure 5: Results of simulations of radial dynamics of an air cavitation bubble (R_o = 10 μm) in cavitating flow downstream of throat in orifice. Time history of: (A) normalized radius (R/R_o) of the bubble, (B) temperature inside the bubble, (C) water vapor molecules in the bubble, and (D) pressure inside the bubble.

Figure 6: Results of the model sonochemical reaction (Iodine yield through KI oxidation) in different cavitation devices. (a) Iodine yield as function of energy dissipated in the flow (samples were collected at 3, 6, 9, 12, 15 & 20 min, see Table 3 for operating parameters), (b) Final iodine yield at end of 20 min treatment.

Figure 7: Photographs of the cavitation clouds generated in downstream region of throat in venturi-1 and venturi-2

Table 1. Equations of the Diffusion-limited Model for Cavitation Bubble Dynamics

Model Component	Equation	Initial Value
1. Radial motion of the cavitation bubble	$\left(1-\frac{dR/dt}{c}\right)R\frac{d^2R}{dt^2}+\frac{3}{2}\left(1-\frac{dR/dt}{3c}\right)\left(\frac{dR}{dt}\right)^2=\frac{1}{\rho_L}\left(1+\frac{dR/dt}{c}\right)(P_i-P_t)+\frac{R}{\rho_L c}\frac{dP_i}{dt}-4\nu\frac{dR/dt}{R}-\frac{2\sigma}{\rho_L R}$ Internal pressure in the bubble: $P_i=\frac{N_{tot}(t)\,kT}{\left[4\pi\left(R^3(t)-h^3\right)/3\right]}$ Pressure in bulk liquid medium: $P_t=\rho_L u_{throat}^2/2+P_{throat}-\rho_L(u_t^{new})^2/2$	At t = 0, $R = R_o$ $dR/dt = 0$
2. Diffusive flux of water vapor molecules	$\frac{dN_W}{dt}=4\pi R^2 D_W\left.\frac{\partial C_W}{\partial r}\right\|_{r=R}\approx 4\pi R^2 D_W\left(\frac{C_{W,R}-C_W}{l_{diff}}\right)$ Instantaneous diffusive penetration depth: $l_{diff}=\min\left(\sqrt{\frac{RD_W}{\lvert dR/dt\rvert}},\frac{R}{\pi}\right)$	At t = 0, $N_W = 0$
3. Heat conduction across bubble wall	$\frac{dQ}{dt}=4\pi R^2\lambda\left.\frac{\partial T}{\partial r}\right\|_{r=R}\approx 4\pi R^2\lambda\left(\frac{T_0-T}{l_{th}}\right)$ Thermal diffusion length: $l_{th}=\min\left(\sqrt{\frac{R\kappa}{\lvert dR/dt\rvert}},\frac{R}{\pi}\right)$	At t = 0, $Q = 0$
4. Overall energy balance	$C_{V,mix}dT/dt=dQ/dt-P_i dV/dt+\left(h_W-U_W\right)dN_W/dt$ Mixture heat capacity: $C_{V,mix}=\sum C_{V,i}N_i$ (i = N_2/ O_2/ water) Molecular properties of water: Enthalpy: $h_W = 4kT_o$ Internal energy: $U_W=N_W kT\left(3+\sum_{i=1}^{3}\frac{\theta_i/T}{\exp(\theta_i/T)-1}\right)$ Heat capacity of various species (i = N_2/ O_2/ water): $C_{V,i}=N_i k\left(f_i/2+\sum\left((\theta_i/T)^2\exp(\theta_i/T)/\left(\exp(\theta_i/T)-1\right)^2\right)\right)$	At t = 0, $T = T_0$

Table 2. Thermodynamic Properties of Various Species in Cavitation Bubble[20-22]

Species	Degrees of freedom (translational + rotational) (f_i)	Lennard–Jones force constants		Characteristic vibrational temperatures θ (K)
		σ (10^{-10} m)	ε/k (K)	
N_2	5	3.68	92	3350
O_2	5	3.43	113	2273
H_2O	6	2.65	380	2295, 5255, 5400

Table 3. Parameters for determination of Pressure Recovery Profile in the Downstream Region of Venturi/Orifice

Flow Geometry	Venturi–1	Venturi–2	Venturi–3	Orifice
Pressure at Throat (kPa)	4.2	4.2	4.2	4.2
P_2 (kPa)	101.3	101.3	101.3	101.3
P_1 (kPa)	427.62	422.12	160.62	233.65
τ (s)	1.60×10^{-3}	2.96×10^{-3}	5.68×10^{-3}	1.82×10^{-3}
$\overline{u'}$ (m/s)	2.55	2.17	1.66	1.3
f_T (kHz)	4.55	3.87	3.18	2.33
u_{pipe} (m/s)	0.81	0.8	7.51	0.6
u_{throat} (m/s)	29.12	28.93	19.23	21.43
Diameter of the inlet pipe (mm)	12	12	8	25
Throat diameter (mm)	2.07	2.22	5.00	2.00
Throat Length (mm)	1	1	2	4
Convergent section (mm) (a)	6	12	24	-
Divergent section(mm) (b)	24	44	76	-
Venturi length (mm) (a + b)	30	57	103	-
Convergent angle (degree)	39	22	2	-
Divergent angle (degree)	12	6	4	-
Flow rate (mL/s)	98	112	378	67
Cavitation number	0.23	0.23	0.53	0.42
Power delivered by pump (W)	31.78	36.31	61.20	21.83
Iodine concentration after 20 min of operation (mg/L)	8.38	9.49	5.54	4.87[C]
Avg. cavitation yield (mg/kJ)	0.115	0.106	0.039	0.165

Table 4. Experimental Conditions

Temperature range	30-35°C
KI initial concentration	2% (wt. basis)
System Volume	6 lit
Sample collection times	0, 3, 6, 9, 12, 15 & 20 min
Iodine measurements	UV spectrophotometer at 354 nm

Table 5. Summary of Simulations of Individual Cavitation Bubble Dynamics in different Cavitation Devices

	Air bubble (initial radius = 10 μm)			
	Venturi – 1	Venturi – 2	Venturi – 3	Orifice
	Conditions at first compression of the bubble			
Species	T_{max} = 6000 K P_{max} = 14250 bar N_W = 3.43E+010 x_{N2} = 0.280 x_{O2} = 0.074 x_W = 0.646	T_{max} = 5897 K P_{max} = 13950 bar N_W = 1.75E+010 x_{N2} = 0.409 x_{O2} = 0.109 x_W = 0.482	T_{max} = 5671 K P_{max} = 12950 bar N_W = 2.19E+010 x_{N2} = 0.365 x_{O2} = 0.097 x_W = 0.538	T_{max} = 5706 K P_{max} = 13770 bar N_W = 4.5E+010 x_{N2} = 0.233 x_{O2} = 0.062 x_W = 0.705
	Equilibrium mole fraction of species in the bubble at transient collapse			
H_2O	2.7864E–03	2.9772E–03	3.5485E–03	3.2845E–03
H_2	6.0099E–04	5.8026E–04	5.6319E–04	5.2385E–04
$OH^•$	1.6224E–02	1.6126E–02	1.6035E–02	1.5492E–02
O_2	8.4615E–02	8.8243E–02	9.4056E–02	9.3699E–02
$H^•$	3.3337E–03	3.0521E–03	2.5837E–03	2.4906E–03
$O^•$	4.7850E–02	4.5117E–02	3.9189E–02	3.9228E–02
$HOO^•$	7.4715E–04	7.5897E–04	7.7087E–04	7.6328E–04
H_2O_2	1.0221E–05	1.0761E–05	1.2013E–05	1.1557E–05
O_3	5.1368E–05	5.1568E–05	4.8826E–05	5.0979E–05
N_2	6.6824E–01	6.6913E–01	6.7519E–01	6.7484E–01
NO	1.7010E–01	1.6876E–01	1.6334E–01	1.6480E–01
NO_2	2.0786E–03	2.1283E–03	2.1519E–03	2.2172E–03
N	1.6150E–03	1.3740E–03	9.5952E–04	9.9182E–04
N_2O	1.1458E–03	1.1185E–03	1.0333E–03	1.0771E–03
HNO	2.6431E–04	2.5448E–04	2.3280E–04	2.3376E–04
NH	1.2242E–04	1.0529E–04	7.6397E–05	7.7410E–05
HNO_2	1.6236E–04	1.6728E–04	1.7390E–04	1.7592E–04
N_3	3.6443E–05	3.0897E–05	2.0999E–05	2.2928E–05
NH_2	1.0316E–05	—	—	—

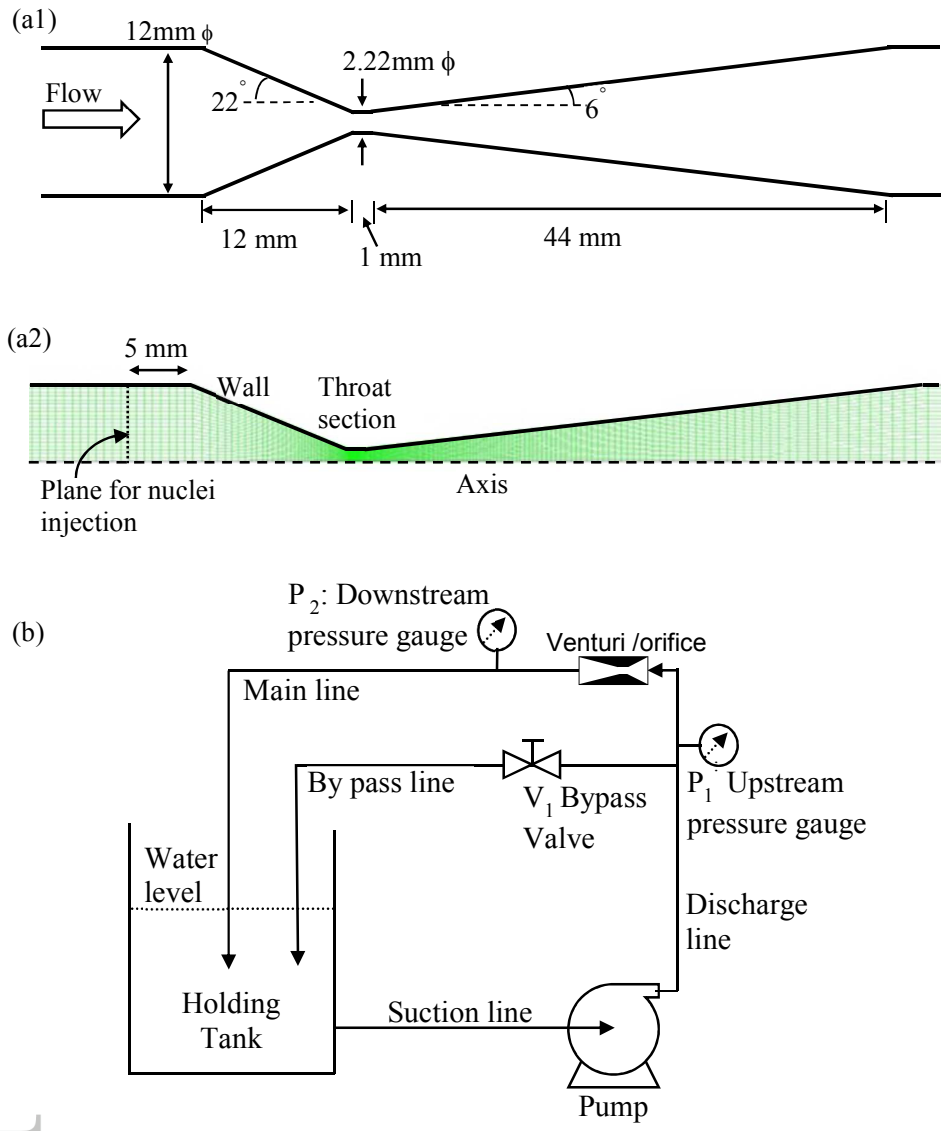

Figure 1. (a.1) Schematic diagram of the venturi 2. (a.2) Mesh used for CFD simulations and plane for nuclei injection. (b) Schematic diagram of the hydrodynamic cavitation closed loop set-up.

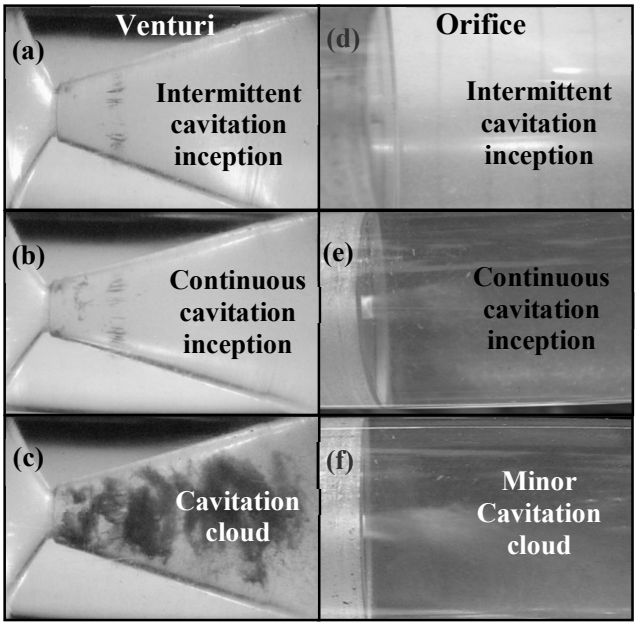

Figure 2. Photographs of cavitating flow downstream of venturi / orifice throat. Inception of cavitation phenomena is visible in (a) and (d) for venturi (for inlet pressure 180 kPa) and orifice (for working inlet pressure 240 kPa), respectively. Fully developed cavitation bubble clouds for the highest inlet pressure of 320 kPa for venturi and orifice are visible in (c) and (f).

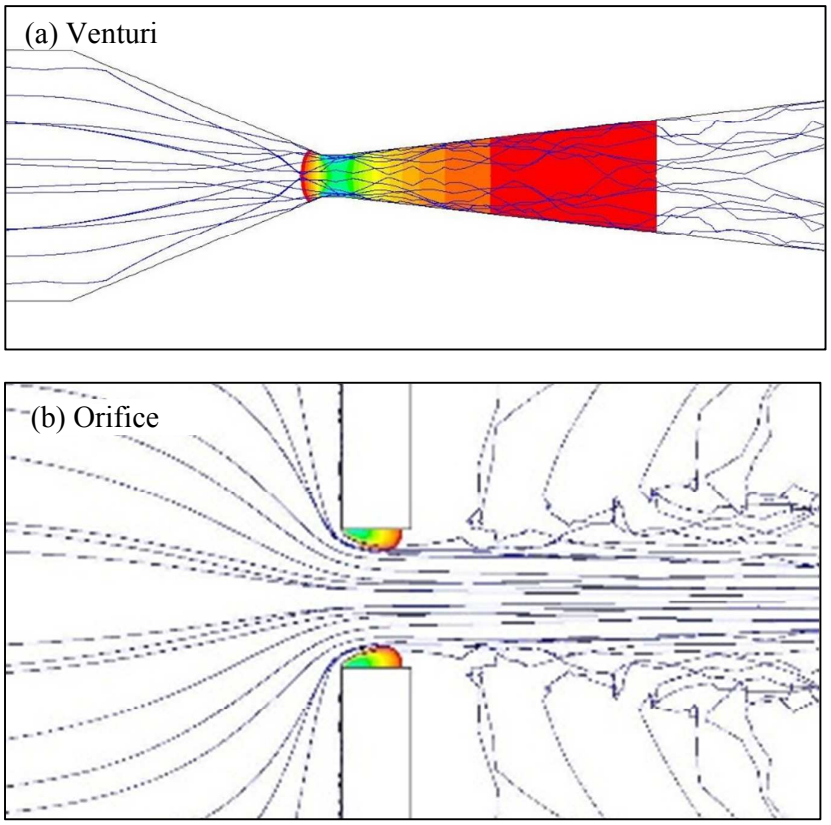

Figure 3. Cavitation bubble paths or trajectories overlapped over the pressure contours in (a) venturi, and (b) orifice. The pressure contours are clipped so that maximum pressure is 50 kPa and minimum pressure is 4 kPa to indicate probable cavitation zone.

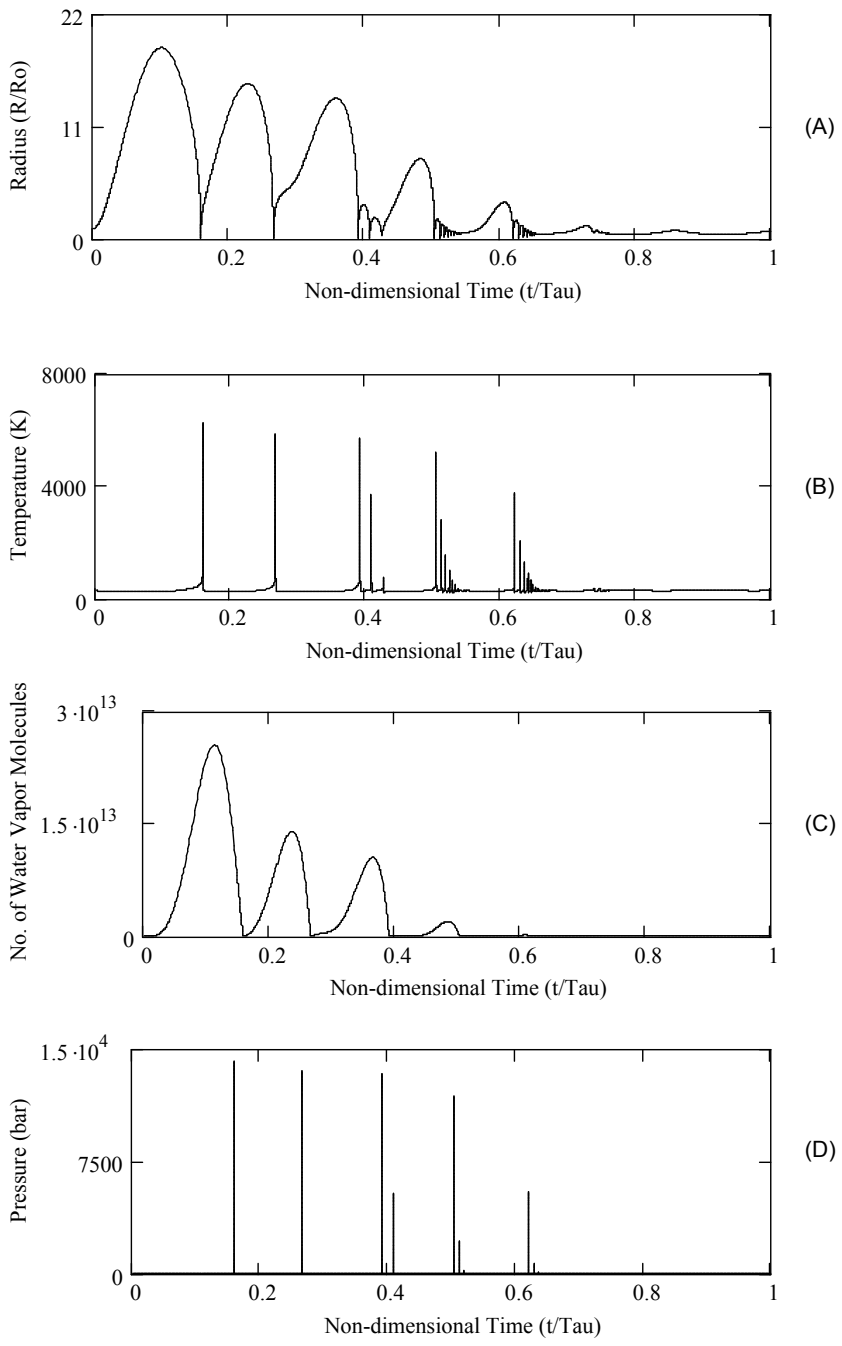

Figure 4. Results of simulations of radial dynamics of an air cavitation bubble (R_o = 10 μm) in cavitating flow downstream of throat in venturi - 1. Time history of: (A) normalized radius (R/R_o) of the bubble, (B) temperature inside the bubble, (C) water vapor molecules in the bubble, and (D) pressure inside the bubble.

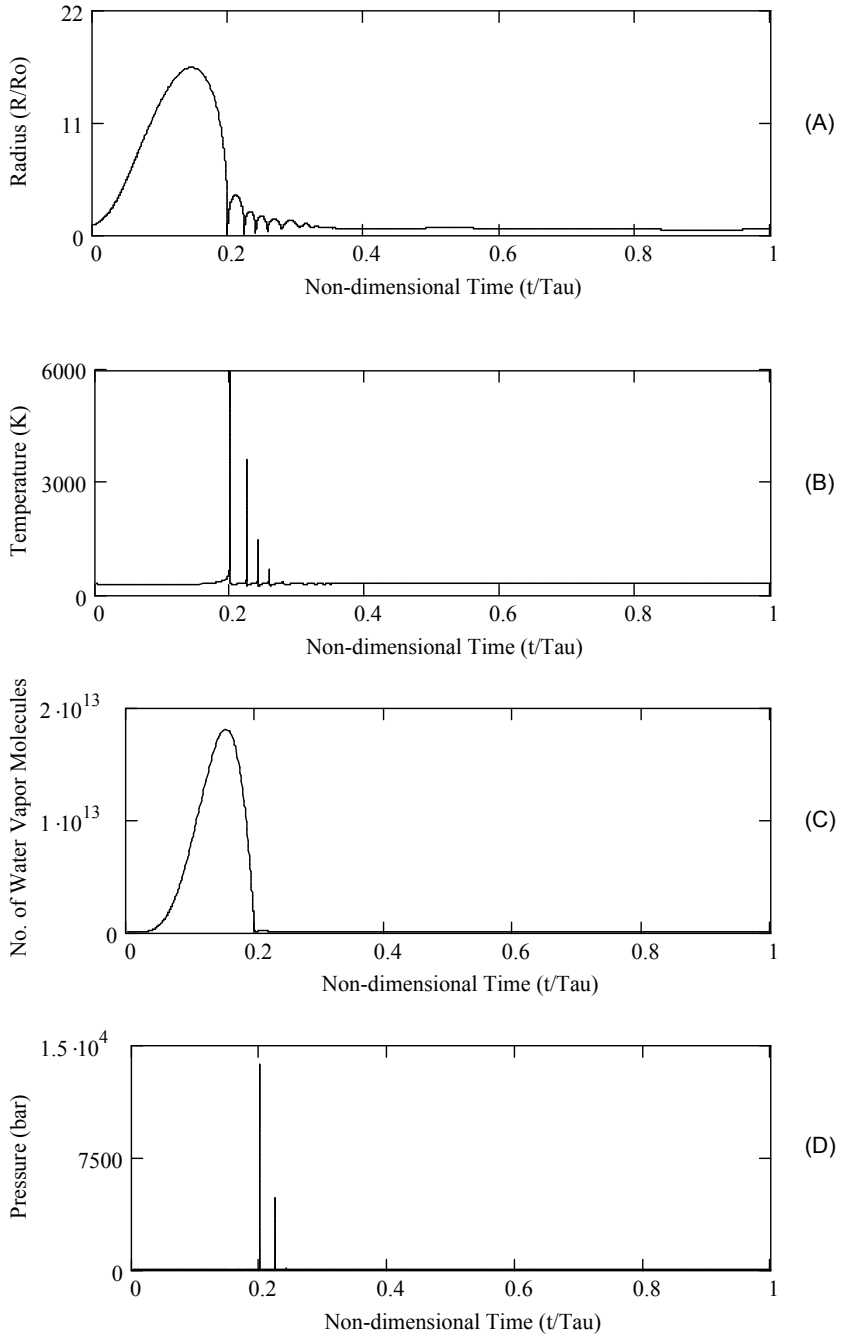

Figure 5. Results of simulations of radial dynamics of an air cavitation bubble (R_o = 10 μm) in cavitating flow downstream of throat in orifice. Time history of: (A) normalized radius (R/R_o) of the bubble, (B) temperature inside the bubble, (C) water vapor molecules in the bubble, and (D) pressure inside the bubble.

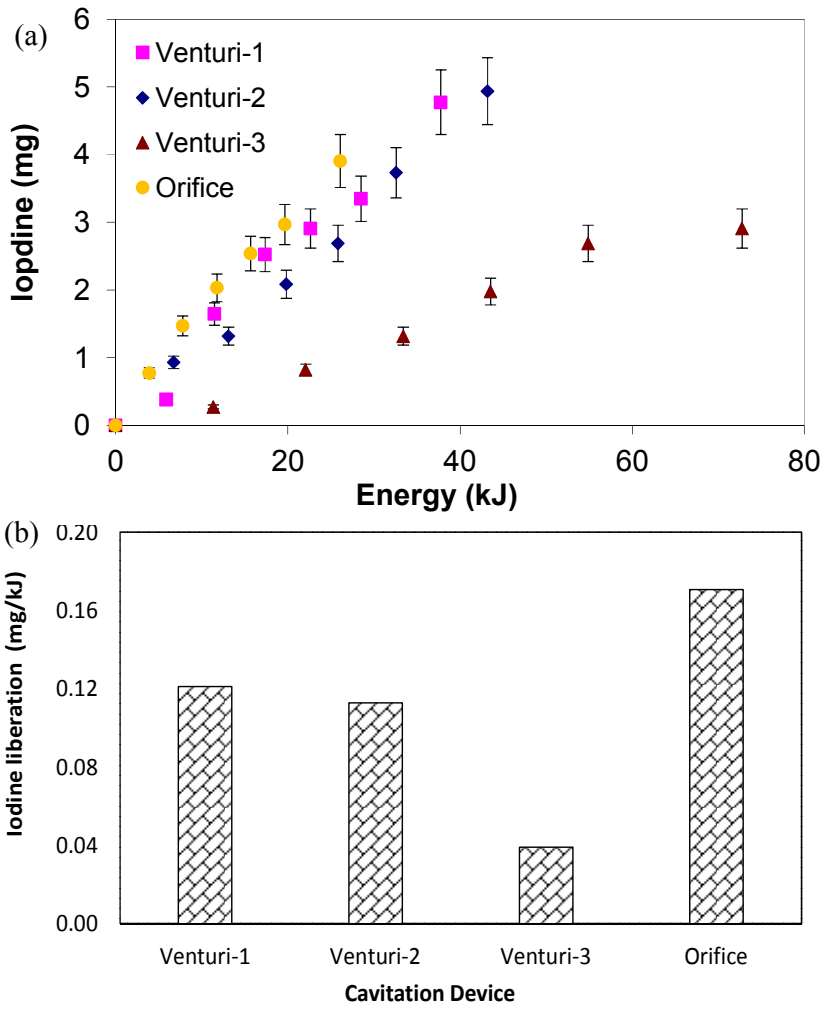

Figure 6. Results of the model sonochemical reaction (Iodine yield through KI oxidation) in different cavitation devices. (a) Iodine yield as function of energy dissipated in the flow (samples were collected at 3, 6, 9, 12, 15 & 20 min, see Table 3 for operating parameters), (b) Final iodine yield at end of 20 min treatment.

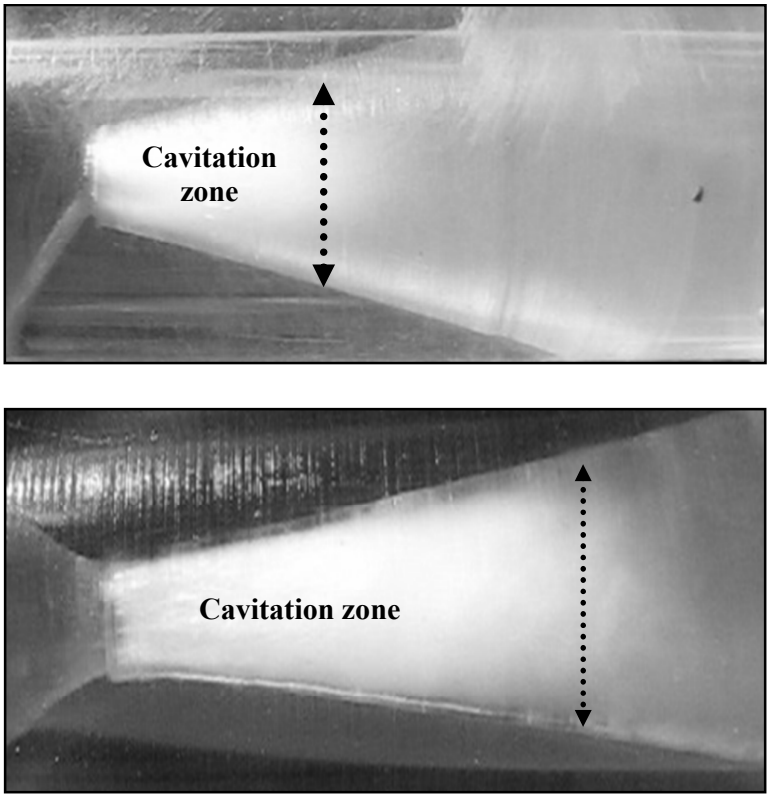

Figure 7. Photographs of the cavitation clouds generated in downstream region of throat in venturi-1 and venturi-2.